

## A CsI(Tl) Scintillating Crystal Detector for the Studies of Low Energy Neutrino Interactions

H.B. Li<sup>a,b</sup>, Y. Liu<sup>c</sup>, C.C. Chang<sup>d</sup>, C.Y. Chang<sup>d</sup>, J.H. Chao<sup>e</sup>, C.P. Chen<sup>a</sup>, T.Y. Chen<sup>f</sup>,  
M. He<sup>g</sup>, L. Hou<sup>h</sup>, G.C. Kiang<sup>a</sup>, W.P. Lai<sup>a</sup>, S.C. Lee<sup>a</sup>, J. Li<sup>c</sup>, J.G. Lu<sup>c</sup>, Z.P. Mao<sup>c</sup>,  
H.Y. Sheng<sup>a,c</sup>, R.F. Su<sup>i</sup>, P.K. Teng<sup>a</sup>, C.W. Wang<sup>a</sup>, S.C. Wang<sup>a</sup>, H.T. Wong<sup>a,1</sup>,  
T.R. Yeh<sup>j</sup>, Z.Y. Zhang<sup>k</sup>, D.X. Zhao<sup>a,c</sup>, S.Q. Zhao<sup>c</sup>, Z.Y. Zhou<sup>h</sup>, B.A. Zhuang<sup>a,c</sup>

The TEXONO<sup>2</sup> Collaboration

<sup>a</sup> Institute of Physics, Academia Sinica, Taipei, Taiwan.

<sup>b</sup> Department of Physics, National Taiwan University, Taipei, Taiwan.

<sup>c</sup> Institute of High Energy Physics, Beijing, China.

<sup>d</sup> Department of Physics, University of Maryland, College Park, U.S.A.

<sup>e</sup> Nuclear Science and Technology Development Center, National Tsing Hua University,  
Hsinchu, Taiwan.

<sup>f</sup> Department of Physics, Nanjing University, Nanjing, China.

<sup>g</sup> Department of Physics, Shandong University, Jinan, China.

<sup>h</sup> Department of Nuclear Physics, Institute of Atomic Energy, Beijing, China.

<sup>i</sup> Nuclear Engineering Division, Nuclear Power Plant II, Kuosheng, Taiwan.

<sup>j</sup> Engineering Division, Institute of Nuclear Energy Research, Lungtan, Taiwan.

<sup>k</sup> Department of Electronics, Institute of Radiation Protection, Taiyuan, China.

---

<sup>1</sup>Corresponding author: Email: htwong@phys.sinica.edu.tw; Tel:+886-2-2789-9682; FAX:+886-2-2788-9828.

<sup>2</sup>Taiwan EXperiment On Neutrino

## Abstract

Scintillating crystal detector may offer some potential advantages in the low-energy, low-background experiments. A 500 kg CsI(Tl) detector to be placed near the core of Nuclear Power Station II in Taiwan is being constructed for the studies of electron-neutrino scatterings and other keV–MeV range neutrino interactions. The motivations of this detector approach, the physics to be addressed, the basic experimental design, and the characteristic performance of prototype modules are described. The expected background channels and their experimental handles are discussed.

**PACS Codes:** 14.60.Pq; 29.40.Mc

**Keywords:** Neutrinos; Scintillation detector

# 1 Introduction

Scintillating crystal detectors [1] have been widely used as electromagnetic calorimeters in high energy physics [2], as well as in medical and security imaging and in the oil-extraction industry. They offer many potentials merits [3] for low-energy (keV-MeV range) low background experiments.

A CsI(Tl) scintillating crystal detector is being constructed to be placed near a reactor core to study low energy neutrino interactions [4]. In subsequent sections, we discuss the motivations for this choice of detector technology, the physics topics to be addressed, the basic experimental design and the prototype performance parameters. The various background processes and the experimental means to identify and suppress them are considered. Various extensions based on this detector technique are summarized at the end.

## 2 Physics and Detector Motivations

High energy (GeV) neutrino beams from accelerators have been very productive in the investigations of electroweak, QCD and structure function physics [5] and have blossomed into matured programs at CERN and Fermilab. However, the use of low energy (MeV) neutrino as a probe to study particle and nuclear physics has not been well explored.

Nuclear power reactors are abundant source of electron anti-neutrinos ( $\bar{\nu}_e$ ) at the MeV range. Previous experiments with reactor neutrinos primarily focused on the interactions

$$\bar{\nu}_e + p \rightarrow e^+ + n$$

to look for neutrino oscillations [6]. The choice of this interaction channel is due to its relatively large cross-sections, the very distinct experimental signatures (prompt  $e^+$  followed by a delayed neutron capture), and the readily available detector choice of liquid scintillator providing the proton target. Using this interaction, the reactor neutrino spectrum has been measured to a precision of  $\sim 2\%$  in the 3 MeV to 7 MeV range from the Bugey experiment [7].

The only other processes measured at the MeV range for  $\bar{\nu}_e$  are  $\bar{\nu}_e$ -electron [8, 9, 10] and  $\bar{\nu}_e$ -deuteron [11] interactions, and their accuracies are at the 30-50% and 10-20% range, respectively. There are motivations to improve on these measurements, to investigate complementary detection techniques, and to study the other unexplored channels.

Gamma-ray spectroscopy has been a standard technique in nuclear sciences (that is, in the investigations of physics at the MeV range), with the use of scintillating crystals or solid-state detectors. Gamma-lines of characteristic energies give unambiguous information on the presence and transitions of whichever specific isotopes, allowing a unique interpretation of both the signal and background processes.

Several intrinsic properties of crystal scintillators make them attractive candidates for low-background experiments [3] in neutrino and astro-particle physics. The experimental difficulties of building a high-quality gamma detector for MeV neutrino physics have been the large target mass required. However, in recent years, big electro-magnetic calorimeter systems [2] (such as the mass of 40 tons of CsI(Tl) crystals, in the case for the current B-factories experiments [12]) have been built for high energy physics experiments, using CsI(Tl) crystals [13] with silicon PIN photo-diodes readout [14]. In addition, NaI(Tl) detectors with the mass range of 100 kg have been used in Dark Matter WIMP searches [15], producing some of the most sensitive results.

The CsI-crystal production technology is by now well matured and the cost has been reduced enormously due to the large demands. It becomes realistic and affordable to build a CsI detector in the range of 1-ton in target mass for a reactor neutrino experiment. The detector is technically much simpler to build and to operate than, for instance, gas chambers and liquid scintillators. The detector mass can be readily scaled up to tens of tons if the first experiment would yield interesting results or lead to other potential applications. Other scintillating crystal detectors can be easily customized in the various potential applications.

The properties of CsI(Tl) crystals, together with those of a few common scintillators, are listed in Table 1. The CsI(Tl) crystal offers certain advantages over the other possibilities. It has relatively high light yield and high photon absorption (or short radiation length). It is mechanically stable and easy to machine, and is only weakly hygroscopic. There is no need for a hermetic container to seal the detector from the ambient humidity (as required, for instance, by NaI(Tl)). This minimizes radioactive background as well as energy loss in the passive elements which will degrade energy resolution. In particular, CsI(Tl) provides strong attenuation for  $\gamma$ 's of energy less than 500 keV. As a result, it is possible to realize a compact detector design with minimal passive materials within the fiducial volume, and with an efficient external shielding configuration.

### 3 Neutrino Interactions on CsI(Tl)

#### 3.1 Neutrino-Electron Scattering

The cross section for the process

$$\bar{\nu}_e + e^- \rightarrow \bar{\nu}_e + e^-$$

gives information on the electro-weak parameters ( $g_V$ ,  $g_A$ , and  $\sin^2\theta_W$ ), and are sensitive to small neutrino magnetic moments ( $\mu_\nu$ ) and the mean square charge radius ( $\langle r^2 \rangle$ ) [16, 17]. Scatterings of the ( $\nu_e e$ ) [19] and ( $\bar{\nu}_e e$ ) are two of the most realistic systems where the interference effects between Z [neutral currents (NC)] and W [charged currents (CC)] exchanges can be studied [18]. Many of the existing and proposed solar neutrino detectors (Super-Kamiokande, Borexino, HELLAZ, HERON ...) [20] make use of the  $\nu_e$ -e interactions as their detection mechanisms. The fact the  $\nu_e$ -e scattering can proceed via both W and Z exchanges, while  $\nu_\mu$ -e and  $\nu_\tau$ -e are purely neutral current processes, is the physics-basis of Resonance Neutrino Oscillation in Matter (the “MSW” Effect) [21].

In an experiment, what can be measured is the recoil energy of the electron (T). The differential cross section can be expressed as :

$$\begin{aligned} \frac{d\sigma}{dT}(\nu e) = & \frac{G_F^2 m_e}{2\pi} [(g_V \pm x \pm g_A)^2 + (g_V \pm x \mp g_A)^2 [1 - \frac{T}{E_\nu}]^2 + (g_A^2 - (g_V \pm x)^2) \frac{m_e T}{E_\nu^2}] \\ & + \frac{\pi \alpha_{em}^2 \mu_\nu^2}{m_e^2} [\frac{1 - T/E_\nu}{T}] \end{aligned}$$

where  $g_V = 2 \sin^2\theta_W - \frac{1}{2}$  and  $g_A = -\frac{1}{2}$  in the Standard Model, while the upper (lower) signs refer to  $\nu_\mu e$  and  $\nu_\tau e$  ( $\bar{\nu}_\mu e$  and  $\bar{\nu}_\tau e$ ) scatterings where only NC are involved, and

$$x = \frac{2M_W^2}{3} \langle r^2 \rangle \sin^2\theta_W .$$

For  $\nu_e e$  scattering, both NC and CC and their interference terms contribute, so that the cross sections can be evaluated by replacing  $g_V \rightarrow g_V + 1$  and  $g_A \rightarrow g_A + 1$ . The  $\mu_\nu$  term have a  $\frac{1}{T}$  dependence. Accordingly, experimental searches for the neutrino magnetic moment should focus on the reduction of the threshold (usually background-limited) for the recoil electron energy.

The  $g_A$  Vs.  $g_V$  parameter space where ( $\bar{\nu}_e e$ ) scatterings are sensitive to is depicted in Figure 1. The complementarity with ( $\nu_\mu e$ ,  $\bar{\nu}_\mu e$ ,  $\nu_e e$ ) can be readily seen. The expected

recoil energy spectrum [17] is displayed in Figure 2a, showing standard model expectations and the case with an anomalous neutrino magnetic moment of  $10^{-10} \mu_B$ . The present published limit [10] is  $1.9 \times 10^{-10} \mu_B$ . The number of events in the two cases as a function of measurement threshold is depicted in Figure 2b. It can be seen that the rate is at the range of O(1) events per kg of CsI(Tl) per day [ $\equiv$  “pkd”]<sup>3</sup> at about 100 keV threshold at a reactor neutrino flux of  $10^{13} \text{ cm}^{-2}\text{s}^{-1}$ , which poses formidable experimental challenge in terms of background control.

Therefore, investigations of  $(\bar{\nu}_e e)$  cross-sections with reactor neutrinos allow one to study electro-weak physics at the MeV range, to probe charged and neutral currents interference, and to look for an anomalous neutrino magnetic moment. The present experimental situations are discussed in Ref. [22] and summarized in Table 2. In particular, a re-analysis [17] of the Savannah River results [8], based on an improved reactor neutrino spectrum and the Standard Model  $\sin^2\theta_W$  value, suggested that the measured  $(\bar{\nu}_e e)$  cross-sections at 1.5-3.0 MeV and 3.0-4.5 MeV are  $1.35 \pm 0.4$  and  $2.0 \pm 0.5$  times, respectively, larger than the expected values, and can be interpreted to be consistent with a  $\mu_\nu$  at the range of  $(2-4) \times 10^{-10} \mu_B$ . Various astrophysics considerations from the time duration of the supernova SN1987A burst [23], stellar cooling [24] and Big Bang Nucleosynthesis [25] provide more stringent bounds on  $\mu_\nu$  to the  $10^{-11} - 10^{13} \mu_B$  level, but these are model-dependent. An anomalous neutrino magnetic moment of range  $\mu_\nu \sim 10^{-10} \mu_B$  has been considered as a solution to the Solar Neutrino Puzzle [26]. There are motivations to improve the cross-section measurements and magnetic moment sensitivities further with laboratory experiments. Several other projects are underway [22, 27].

A 500 kg CsI(Tl) crystal calorimeter (fiducial mass 200-300 kg) will have more target electrons than previous experiments [8, 9, 10] and current projects [22, 27], as shown in Table 2. The signature for  $(\bar{\nu}_e e)$  will be a single hit out of the several hundred channels. As discussed in Section 6, the crystal scintillator approach may provide low detection threshold, high photon attenuation, and powerful diagnostic capabilities for background understanding. All these features can potentially improve the sensitivities for both cross-section measurements and magnetic moments studies.

---

<sup>3</sup>For simplicity, we denote “events per kg of CsI(Tl) per day” by **pkd** in this article.

## 3.2 Neutrino Interactions on $^{133}\text{Cs}$ and $^{127}\text{I}$

Neutral current excitation (NCEX) on nuclei by neutrinos

$$\bar{\nu}_e + (A, Z) \rightarrow \bar{\nu}_e + (A, Z)^*$$

has been observed only in the case of  $^{12}\text{C}$  [28] with intermediate energy ( $O(10 \text{ MeV})$ ) neutrinos. Excitations with lower energies using reactor neutrinos have been studied theoretically [29] but not observed.

Crystal scintillators, having good  $\gamma$  resolution and capture efficiency, are suitable to study these processes. The experimental signatures will be an excess of events at the characteristic gamma-energies correlated to the Reactor-ON period. Using CsI(Tl) as active target nuclei, the candidate  $\gamma$ -lines with M1 transitions include 81 and 160 keV for  $^{133}\text{Cs}$ , and 58, 202 and 418 keV for  $^{127}\text{I}$ . The use of NCEX as the detection mechanisms for solar neutrinos [30, 31] and Dark Matter-WIMPs [32] have been discussed. Competitive limits have been set with the WIMP-searches based on the NCEX channel with  $^{127}\text{I}$  [33] and  $^{129}\text{Xe}$  [34].

There are no theoretical predictions for these transitions for  $^{133}\text{Cs}$  and  $^{127}\text{I}$ . One may expect a similar range as the 480 keV case for  $^7\text{Li}$  [29], which would be  $O(0.01\text{-}0.1) \text{ pkd}$  at a reactor neutrino flux of  $10^{13} \text{ cm}^{-2}\text{s}^{-1}$ . In addition, there are theoretical work [35] suggesting that the NCEX cross-sections on  $^{10}\text{B}$  and  $^{11}\text{B}$  are sensitive to the axial isoscalar component of NC interactions and the strange quark content of the nucleon. The studies of neutrino-induced interactions on nuclei is one of the principal program of the ORLaND proposal [36] based on intermediate energy neutrinos from spallation neutron source.

For completeness, we mention that  $\bar{\nu}_e$  can also interact with  $^{133}\text{Cs}$  and  $^{127}\text{I}$  via the charged-current (CC) channels. There are two modes: (I) Inverse beta decay

$$\bar{\nu}_e + (A, Z) \rightarrow e^+ + (A, Z - 1)^*$$

have the distinct signatures of 2 back-to-back 511 keV  $\gamma$ s from the positron annihilation, plus the characteristic  $\gamma$ -lines from the daughter nuclei, and the positron itself; (II) Resonant orbital electron capture

$$\bar{\nu}_e + e^- + (A, Z) \rightarrow (A, Z - 1)^*$$

takes place only at a narrow range of neutrino energy equal to the Q-value of the transition. The signatures are the characteristic gamma lines for the excited daughter nuclei. Calculation does not exist but the event rates are expected to be further suppressed since

they involve the conversion of a proton to a neutron in neutron-rich nuclei. The  $\bar{\nu}_e$ N-CC interactions have been considered to detect the low-energy terrestrial neutrinos due to the radioactivity at the Earth’s lithosphere [37].

## 4 Experimental Design

Since mid-1997, a Collaboration has been built up [38] to pursue an experimental program discussed in Section 3 – the studies of low energy neutrino interactions using reactor neutrinos as source with CsI(Tl) crystal as detector [4].

The experiment will be performed at the Nuclear Power Station II at Kuo-sheng at the northern shore of Taiwan. The experimental location is about 28 m from one of the reactor cores, and 102 m from the other one. Each of the cores is a boiling water reactor with 2.9 GW thermal power output, giving a total flux of about  $5.6 \times 10^{12} \text{ cm}^{-2}\text{s}^{-1}$  at the detector site. The site is at the lowest level of the reactor building, with about 25 mwe of overburden, as depicted schematically in Figure 3.

To fully exploit the advantageous features of the scintillating crystal approach [3] in low-energy low-background experiments, the experimental configuration should enable the definition of a fiducial volume with a surrounding active  $4\pi$ -veto, and minimal passive materials.

The schematic design of the experiment is shown in Figure 4. The detector will consist of about 480 kg of CsI(Tl) crystals<sup>4</sup>, arranged in a  $17 \times 15$  matrix. One CsI(Tl) crystal unit consists of a hexagonal-shaped cross-section with 2 cm side and a length 20 cm, giving a mass of 0.94 kg. Two such units are glued optically at one end to form a module. The light output are read out at both ends by 29 mm diameter photo-multipliers (PMTs) with low-activity glass window<sup>5</sup>, which provide about 50% of end-surfaces coverage. The design of the PMT base is optimized for high gain (low threshold) and good linearity over a large dynamic range. The modular design enables the detector to be constructed in stages.

Individual crystals are wrapped with 4 layers of 70  $\mu\text{m}$  thick teflon sheets to provide diffused reflection for optimal light collection. The sum of the two PMT signals ( $Q_{\text{tot}} = Q_1 + Q_2$ ) gives the energy of the event, while the difference will provide a measurement of a longitudinal position. Outer layers as well as the last few cm near the

---

<sup>4</sup>Manufacturer: Unique Crystals, Beijing

<sup>5</sup>Hamamatsu CR110 customized



readout surfaces will be used as active veto. The exact definitions of fiducial and veto volume can be fine-tuned based on the actual background, and can differ with different energy ranges.

The schematics of the electronics system is depicted in Figure 5. The PMT signals are fed to amplifiers and shapers, and are finally digitized by 8-bit Flash-Analog-Digital-Convertor (FADC) modules running at a clock rate of 20 MHz. The shaping is optimized for the  $\mu\text{s}$  time-scale rise and fall times, such that noise-spikes from single photo-electron are smeared out and suppressed. Typical scintillation pulses due to  $\gamma$  and  $\alpha$  events as measured by the system are displayed in Figure 6. A precision pulse generator provides means to calibrate and monitor the performance and stability of the electronics system.

The trigger conditions include: (a) having any one or more channels above a pre-set “high threshold” (typically 50-100 keV equivalent), and (b) not having a cosmic veto signal within a previous time-bin of typically 100  $\mu\text{s}$ . Once these conditions are fulfilled, all channels with signals above a “low threshold” (typically 10-30 keV equivalent) will be read out. The logic control circuit enables complete acquisition of delayed signatures up to several ms, to record cascade events in decay series like  $^{238}\text{U}$  and  $^{232}\text{Th}$ .

The FADC, the trigger units, logic control and calibration modules, are read out and controlled by a VME-based data acquisition system, connected by a PCI-bus to a PC running with the LINUX operating system. The on-line and off-line software architecture, together with their inter-connections, are shown schematically in Figure 7. The on-site data taking conditions can be remotely monitored from the home-base laboratories via telephone line. (Internet access to the Nuclear Power Plant is not allowed.) Data will be saved in hard disks on-site and replaced at the once-per-week interval. They are duplicated and stored in magnetic tapes and CDs for subsequent off-line analysis. The detailed design and performance of the electronics, data acquisition and control systems will be the subject of a forthcoming article.

The compact CsI(Tl) detector enables an efficient shielding to be built. The schematics of the shielding configuration is depicted in Figure 8. Cosmic-rays and their related events will be vetoed by an outermost layer of plastic scintillators. The typical veto gate-time will be  $\sim 100 \mu\text{s}$  to allow for delayed signatures due to neutron interactions. Ambient radioactivity is suppressed by 15 cm of lead and 5 cm of steel. The steel layer also provides the mechanical structures to the system. Neutrons, mostly cosmic-induced in the lead and steel, are slowed down and then absorbed by 25 cm of boron-loaded polyethylene. The inner 5 cm of oxygen-free-high-conductivity (OFHC) copper serves to suppress residual radioactivity from the shielding materials. The copper layers can

be dismantled and replaced by more polyethylene, allowing flexibilities to optimize the shielding conditions with respect to different physics focus. The CsI(Tl) target will be placed inside a electrically-shielded and air-tight box made of copper sheet. The entire inner target space will be covered by a plastic bag flushed with dry nitrogen to prevent the radioactive radon gas from diffusing into the target region.

To enable detector access and maintenance, the entire shielding assembly consists of three parts: (1) a fixed shielding house, (2) a movable trolley on which the target detector sits, and (3) the front door which can be moved by wheels. All the access pipes and cable trays are bent so that there are no direct line-of-sight between the inner target and the external background. Ports are provided to allow insertion of radiation sources for regular monitoring and calibration. These ports are blocked by copper plugs during normal data taking.

## 5 Performance of Prototype Modules

Extensive measurements on the crystal prototype modules have been performed. The response is depicted in Figure 9, showing the variation of collected light for  $Q_1$ ,  $Q_2$  and  $Q_{\text{tot}}$  as a function of position within one crystal module. The charge unit is normalized to unity at the  $^{137}\text{Cs}$  photo-peak (660 keV) for both  $Q_1$  and  $Q_2$  at their respective ends, while the error bars denote the FWHM width at that energy. The discontinuity at  $L=20$  cm is due to the optical mis-match between the glue ( $n=1.5$ ) and the CsI(Tl) crystal ( $n=1.8$ ). It can be seen that there is a dependence of  $Q_{\text{tot}}$  with position at the 10-20% level. A FWHM energy resolution of 10% is achieved at 660 keV, and its variation with energy follows the  $E^{-\frac{1}{2}}$  relation. The detection threshold (where signals are measured at both PMTs) is  $<20$  keV. A good linearity of the PMT response is achieved for energies from 20 keV to 20 MeV.

The longitudinal position can be obtained by considering the dimensionless ratio  $R = (Q_1 - Q_2)/(Q_1 + Q_2)$ , the variation of which at the  $^{137}\text{Cs}$  photo-peak energy along the crystal length is displayed in Figure 10. The ratio of the RMS errors in  $R$  relative to the slope gives the longitudinal position resolutions. The measured resolutions are 2 cm, 3.5 cm and 8 cm at 660 keV, 200 keV and 30 keV, respectively. The dependence of  $R$  on energy is negligible at the less than the  $10^{-3}$  level.

In addition, CsI(Tl) provides powerful pulse shape discrimination (PSD) properties [39] to differentiate  $\gamma/e$  events from those due to heavily ionizing particles like  $\alpha$ 's,

which have faster fall time, as shown in Figure 6. The typical separation between  $\alpha/\gamma$  in CsI(Tl) with the “Partial Charge Vs Total Charge” method [40] is depicted in figure 11, demonstrating an excellent separation of  $>99\%$  above 500 keV. Unlike in liquid scintillators,  $\alpha$ ’s are only slightly quenched in their light output in CsI(Tl). The quenching factor depends on the Tl concentration and the measurement parameters like shaping time: for full integration of the signals, the suppression is typically 50% [13].

## 6 Background Considerations

### 6.1 Merits of Crystal Scintillator

The suppression, control and understanding of the background is very important in all low background experiments. The scintillating crystal detector approach offers several merits [3] to these ends. The essence are:

#### I. Large Photon Attenuation:

With its high-Z nuclei, CsI(Tl) provides very good attenuation to  $\gamma$ -rays, especially at the low energy range below 500 keV. For instance, the attenuation lengths for a 100 keV  $\gamma$ -ray are 0.12 cm and 6.7 cm, respectively, for CsI(Tl) and liquid scintillator. That is, 10 cm of CsI(Tl) has the same attenuating power as 5.6 m of liquid scintillator at this low energy. Consequently, the effects of external ambient  $\gamma$  background, like those from the readout device, electronics components, construction materials and radon diffusion are negligible after several cm of active veto layer. Therefore, the background at low energy will mostly originate within the fiducial volume due to the internal components.

For CsI(Tl) which is non-hygroscopic and does not need a hermetic seal system to operate, “*internal components*” include only two materials: the crystal itself and the teflon wrapping sheets, typically at a mass ratio of 1000:1. Teflon is known to have very high radio-purity (typically better than the ppb level for the  $^{238}\text{U}$  and  $^{232}\text{Th}$  series) [41]. As a result, the experimental challenge becomes much more focussed - the control and understanding of the internal radio-purity and long-lived cosmic-induced background of the CsI(Tl) crystal itself.

#### II. Characteristic Detector Response:

The detection threshold is lower while the energy resolution of CsI(Tl) is better than typical liquid and plastic scintillator with the same modular mass. Furthermore, in

an O(100 kg) CsI(Tl) detector system, the keV-MeV photons originated within the crystal will be fully captured. These features, together with PSD capabilities for  $\alpha$ -particles and the granularity of the detector design, can provide important diagnostic tools for understanding the physical processes of the system. Once the background channels are identified, understood and measured, subtraction of its associated effects can be performed.

When the dominant background contributions are from internal contaminations, two complementary strategies can be deployed for the background control : (I) consistent background subtraction, using the measured spurious  $\alpha$  or  $\gamma$  peaks which indicates residual radioactivity inside the crystal, and (II) the conventional Reactor ON–OFF subtraction.

The background count rate will be stable and not affected by external parameters such as ambient radon concentrations, details of the surrounding equipment configurations and cosmic veto inefficiencies. Consequently, the systematic uncertainties can be reduced, and the reliabilities of both background suppression processes will be more robust. In addition, the large target mass helps to reduce statistical uncertainties. Spectral shape distribution can also be analyzed to provide additional handles. For instance the comparison of the signal rates between the “< 1 MeV” and the “> 1 MeV” samples can enhance the sensitivities in the magnetic moments studies.

## 6.2 Background Channels

The merits discussed above allow a compact detector design and hence, efficient and cost-effective shielding configurations. While care and the standard procedures are adopted for suppressing the ambient radioactivity background (radon purging, choice of clean construction materials, photon-counting measurements with germanium detectors, use of PMT with low-activity glass), the key background issue remains that of *internal* background from the CsI(Tl) itself. The different contributions and their experimental handles are discussed below.

### 6.2.1 Internal Intrinsic Radioactivity

Unlike in liquid scintillators,  $\alpha$ ’s are only slightly quenched in their light output in CsI(Tl). Crystals contaminated by uranium or thorium would give rise to multiple peaks above 3 MeV, as reported in Ref. [42]. The absence of multiple peak structures in our prototype crystals suggest a  $^{238}\text{U}$  and  $^{232}\text{Th}$  concentration of less than the  $10^{-12}$  g/g level [ $\sim 1$  pkd],

assuming the decay chains are in equilibrium. In addition, direct counting method with a high-purity germanium detector shows the  $^{40}\text{K}$  and  $^{137}\text{Cs}$  contaminations of less than the  $10^{-10}$  g/g [ $\sim 1700$  pkd] and  $4 \times 10^{-18}$  g/g [ $\sim 1200$  pkd] levels, respectively. Mass spectrometry method sets limits of  $^{87}\text{Ru}$  to less than  $8 \times 10^{-9}$  g/g [ $\sim 210$  pkd].

Internal radioactivity background typically consists of  $\alpha$ ,  $\beta$  and  $\gamma$  emissions which have characteristic energies and temporal-correlations. Residual background below the measured limits can be identified and subtracted off based on the on-site data. By careful studies of the timing and energy correlations among the distinct  $\alpha$  signatures, precise information can be obtained on the radioactive contaminants in the cases where the  $^{238}\text{U}$  and  $^{232}\text{Th}$  decay series are not in equilibrium, so that the associated  $\beta/\gamma$  background can be accounted for accurately. For instance, Dark Matter experiments with NaI(Tl) reported trace contaminations (range of  $10^{-18} - 10^{-19}$  g/g [25-250 pkd] of  $^{210}\text{Pb}$  in the detector, based on  $\gamma$ -peak at 46.5 keV and the equivalent peak for  $\alpha$ 's at 5.4 MeV [15, 33]. Accordingly,  $\beta$ -decays from  $^{210}\text{Bi}$  can be subtracted off from the signal. Similarly, the residual  $\beta$ -decays of  $^{40}\text{K}$  and  $^{137}\text{Cs}$  can be accounted for based on their respective characteristic  $\gamma$ -lines measure-able from the data.

### 6.2.2 Cosmic-Induced Radioactivity

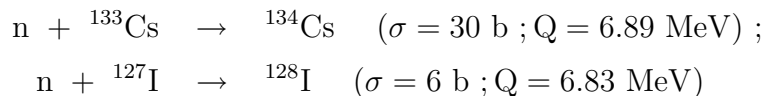
The experiment is located at a site with 25 mwe overburden, which is sufficient to effectively attenuate the primary hadronic component from cosmic rays. The “prompt” cosmic events can be easily identified, since: (a) the plastic scintillator veto can tag them at better than 95% efficiency, (b) bremsstrahlung photons from cosmic-rays on the shieldings cannot reach the inner fiducial volume of the target, as explained in Section 6.1, (c) cosmic-induced neutrons, mostly from the lead, are attenuated and absorbed efficiently by the boron-loaded polyethylene layers, and (d) background originated from cosmic-rays traversing the CsI(Tl) target will lead to unmistakably large pulses ( $\sim 20$  MeV for one crystal).

The more problematic background are due to the long-lived (longer than ms) unstable isotopes created by the various nuclear interaction processes:

#### 1. Neutron Capture

Ambient neutrons or those produced at the the lead shieldings have little probability of being captured by the CsI crystal target, being attenuated efficiently by the boron-loaded polyethylene. Cosmic-induced neutrons (energy range MeV) originated from

the target itself have high probability of leaving the target. Residual neutrons can be captured by the target nuclei  $^{133}\text{Cs}$  and  $^{127}\text{I}$  predominantly via  $(n,\gamma)$  [43]



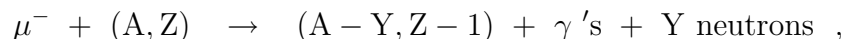
with relatively large cross-sections.

The daughter isotope  $^{134}\text{Cs}$  ( $\tau_{\frac{1}{2}} = 2.05 \text{ yr}$  ;  $Q = 2.06 \text{ MeV}$ ) decays with 70% branching ratio by beta-decay (end point 658 keV), plus the emission of two  $\gamma$ 's (605 keV and 796 keV), and therefore will not give rise to a single hit at the low-energy region. The isotope  $^{128}\text{I}$  ( $\tau_{\frac{1}{2}} = 25 \text{ min}$  ;  $Q = 2.14 \text{ MeV}$ ), on the other hand, has a branching ratio of 79% having a lone beta-decay, which will mimic the single-hit signature. The neutron production rate on-site at the CsI(Tl) target is estimated to be about 50 pkd. Folding in the capture efficiency by the target ( $\sim 25\%$ ) and by  $^{127}\text{I}$  in particular ( $\sim 14\%$ ), the  $^{128}\text{I}$  production rate is about 1.8 pkd.

The neutron capture rate by the CsI target can be measured by tagging  $\gamma$ -bursts of energy 6.8 MeV. Knowing the capture rate, the contributions to the low-energy background due to  $^{128}\text{I}$  can be evaluated and subtracted off. Furthermore, the three-fold coincidence from the  $^{134}\text{Cs}$  decays can be measured, providing additional information to the neutron capture rates.

## 2. Muon Capture

Cosmic-muons can be stopped by the target nuclei and subsequently captured [44] via



where  $Y$  can be 0,1,2,..... with  $\langle Y \rangle \sim 1.2$ . The daughter isotopes for  $Y=1,2,3$  are all stable, while the  $Y=0$  case (less than 5% probability) will give rise to  $^{133}\text{Xe}$  and  $^{127}\text{Te}$ , both of which can lead to low-energy single-site background events:  $^{133}\text{Xe}$  ( $\tau_{\frac{1}{2}} = 5.3 \text{ days}$  ;  $Q = 428 \text{ keV}$ ) decays with beta (end-point 347 keV) plus a  $\gamma$ -ray at 81 keV, while  $^{127}\text{Te}$  ( $\tau_{\frac{1}{2}} = 9.4 \text{ hr}$  ;  $Q = 690 \text{ keV}$ ) decays with a lone beta. The estimated muon capture rate on-site at the CsI target is  $\sim 30 \text{ pkd}$ , so that the background contributions from the  $Y=0$  channels are less than 1.5 pkd.

## 3. Muon-Induced Nuclear Dissociation

Cosmic-muons can disintegrate the target nuclei via the  $(\gamma,n)$  interactions or by spallations [45], at an estimated rate of  $\sim 10 \text{ pkd}$  and  $\sim 1 \text{ pkd}$ , respectively. Among

the various decay configurations of the final states nuclei of the  $(\gamma, n)$  processes,  $^{132}\text{Cs}$  and  $^{126}\text{I}$ , only about 20% (or  $\sim 2$  pkd) of the cases will give rise to single-hit background. The other decays give characteristic and identifiable signatures. For instance,  $^{132}\text{Cs}$  decays by electron capture resulting in the emissions of a  $\gamma$ -ray at 668 keV plus the X-rays from xenon. These can easily be tagged and used as reference to subtract the single-hit background.

### 6.2.3 Reactor-ON Correlated Background

Previous experiments with reactor neutrinos [6] as well as on-site measurements indicate that  $\gamma$  and neutron background associated with “reactor-ON” are essentially zero outside the reactor core and within reasonable shieldings. The target region is proton-free and therefore neutrino-induced background from  $\bar{\nu}_e\text{-p}$  is negligible. These interactions, however, will occur at the polyethylene shieldings. The prompt  $e^+$  will only give rise at most to 511 keV  $\gamma$ -rays, while the neutron (energy range 1-10 keV) will be mostly captured by the  $^{10}\text{B}$  in the polyethylene, producing only 480 keV  $\gamma$ -rays. Both of these low energy  $\gamma$ -background will be efficiently attenuated by the copper shielding and the active veto.

## 6.3 Sensitivity Goals

From the various background considerations discussed in the previous sections, it can be seen that while the background control is non-trivial like all other low-energy neutrino experiments, there are more experimental handles to suppress and identify them with the crystal scintillator approach. The efficient  $\gamma$ -peak detection, the fine granularity and the PSD capabilities of the CsI(Tl) detector provides enhanced analyzing and diagnostic power for the background understanding. The dominating contribution to the sensitivities is due to the internal background in the CsI(Tl) target. The experimental challenge is focussed and therefore more elaborate procedures can be deployed to study and enhance the radio-purity of this one material as the experiment evolves.

The present studies place limits on internal radio-purity to the range of less than the 1000 pkd level. Residual contaminations, if exist, can be further studied and measured by various methods like photon counting with germanium detectors, neutron activation analysis, mass spectroscopy analysis, as well as by the spectroscopic and time-correlation input from on-site data taking. The effects due to cosmic-induced long-lived isotopes are typically at the range of a few pkd. Background due to both channels can be reduced

by consistent background subtraction when the sources are identified and measured, and the goal of a suppression factor of  $10^2$  can be achieve-able. Such background subtraction strategies have been successfully used in accelerator neutrino experiments. As an illustration, the CHARM-II experiment measured about 2000 neutrino-electron scattering events from a sample of candidate events with a factor of 20 larger in size [49]. Events due to the various background processes were identified and subtracted off, such that a few % uncertainty in the signal rate had been achieved.

It can be seen from Figure 2b that a Standard Model rate of  $\sim 1$  pkd can be expected for a detection threshold of 100 keV. After performing the consistent background suppression, a residual Background-to-Signal ratio of less than 10 before Reactor ON–OFF subtraction is realistic. Therefore, based on Reactor ON/OFF periods of 100 and 50 days, respectively, a fiducial mass of 300 kg of CsI(Tl) target, and a detector systematic uncertainty of 1% in performing the Reactor ON–OFF subtraction, the sensitivity goals of  $3 \times 10^{-11} \mu_B$  for the magnetic moment search and a 5-10% uncertainty to the cross-section measurements can be projected. A comparison with previous on-going experiments is summarized in Table 2.

Under similar assumptions, an event rate of  $>0.005$  pkd can be observed for the  $\bar{\nu}_e$ -NCEX channel of the various candidate lines in the 50-500 keV range, corresponding to the cross-section sensitivities of  $\sim 2 \times 10^{-45} \text{cm}^2$ .

## 7 Status and Prospects

By the end of 1999, the design and prototype studies of the experiment have been completed. Construction is intensely underway. A complete 100-kg system, with full electronics and shieldings, is expected to be installed on-site at the Reactor Plant by summer 2000. Data taking will commence while the second 100-kg system will be added in phase. Future upgrades and modifications of the experiment will depend on the first results, with the goals of achieving a 500 kg system eventually.

The detector design adopted in this experiment can be adopted for other low-energy low-background experiments based on scintillating crystal detectors [3], such as Dark Matter WIMP searches [15, 32], sub-MeV Solar Neutrino detection (indium-loaded [46], LiI(Eu) [31] or GSO [47] crystals have been proposed), and further studies of  $\bar{\nu}_e$ -NCEX on other isotopes like  $^7\text{Li}$ ,  $^{10}\text{B}$  and  $^{11}\text{B}$  [30, 35]. Experience and results from the reactor neutrino experiment with CsI(Tl) crystals reported in this work will provide valuable



input to these projects.

Much flexibility is available for detector optimization based on this generic and easily scale-able design. Different modules can be made of different crystals. More and longer crystals can be glued to form one module. Different crystals can be glued together, in which case the event location among the various crystals can be deduced from the different pulse shape. Passive target can be inserted to replace a crystal module. New wrapping materials can be used instead of teflon – there is an interesting new development with sol-gel coating which can be as thin as a few microns [48], thereby even reducing the passive materials within the fiducial volume further.

The authors are grateful to the technical staff of their institutes for the invaluable support, and to the CYGNUS Collaboration for the loan of the veto plastic scintillators. This work was supported by contracts NSC 87-2112-M-001-034 and NSC 88-2112-M-001-007 from the National Science Council, Taiwan, as well as NSF 01-5-23336 and NSF 01-5-23374 from the National Science Foundation, U.S.A.

## References

- [1] For a recent review on the crystal scintillator detector, see, for example, M. Ishii and M. Kobayashi, Prog. Crystal Growth and Charact., **23**, 245 (1991), and references therein.
- [2] For a recent review on the applications of crystal scintillator in particle physics, see, for example G. Gratta, H. Newman, and R.Y. Zhu, Ann. Rev. Nucl. Part. Sci. **44**, 453 (1994).
- [3] H.T. Wong et al., hep-ex/9910002, submitted to Astropart. Phys.
- [4] H.T. Wong and J. Li, Nucl. Phys. **B** (Proc. Suppl.) **77**, 177 (1999)
- [5] For a recent review on experiments on high energy neutrino interactions, see, for example, J.M. Conrad, M.H. Shaevitz and T. Bolton, Rev. Mod. Phys. **70**, 1341 (1998).
- [6] G. Zacek et al., Phys. Rev. **D 34**, 2621 (1986) ;  
A.I. Afonin et al., Sov. Phys. JETP **67** (2), 213 (1988);  
G.S. Vidyakin et al., JETP Lett. **59**, 364 (1994);  
B. Achkar et al., Nucl. Phys. **B 434**, 503 (1995);  
Z.D. Greenwood et al., Phys. Rev. **D 53**, 6054 (1996);  
M. Apollonio et al., Phys. Lett. **B 420**, 397 (1998);  
F. Boehm et al., Palo Verde Proposal (1993).
- [7] B. Achkar et al., Bugey Collaboration, Phys. Lett. **B 374**, 243 (1996).
- [8] F. Reines, H.S. Gurr and H.W. Sobel, Phys. Rev. Lett. **37**, 315 (1976).
- [9] G.S. Vidyakin et al, JETP Lett. **55**, 206 (1992).
- [10] A.I. Derbin et al., JETP Lett. **57**, 769 (1993).
- [11] T.L. Jenkins, F.E. Kinard, and F. Reines, Phys. Rev. **185**, 1599 (1969); E. Pasierb et al., Phys. Rev. Lett. **43**, 96 (1979);  
G.S. Vidyakin et al., JETP Lett. **49**, 151 (1988); G.S. Vidyakin et al., JETP Lett. **51**, 279 (1990);  
S.P. Riley et al., Phys. Rev. **C 59**, 1780 (1999).

- [12] Letter of Intent, Belle Coll., KEK (1993);  
Letter of Intent, BaBar Coll., SLAC-443 (1994).
- [13] H. Grassman, E. Lorentz, and H.G. Moser, Nucl. Instrum. Methods **228**, 323 (1985);  
P. Schotanus, R. Kamermans, and P. Dorenbos, IEEE Trans. Nucl. Sci. **37**, 177 (1990).
- [14] D.E. Groom, Nucl. Instrum. Methods **219**, 141 (1984);  
S. Gunji et al., Nucl. Instrum. Methods **A 295**, 400 (1990);  
M. Suffert, Nucl. Instrum. Methods **A 322**, 523 (1992).
- [15] K. Fushimi et al., Phys. Rev. **C 47**, R425 (1993);  
M.L. Sarsa et al., Nucl. Phys. **B 35**, 154 (1994);  
N.J.C. Spooner et al., Phys. Lett. **B 321**, 156 (1994);  
R. Bernabei et al., Phys. Lett. **B 450**, 448 (1999);  
G. Gerbier et al., Astropart. Phys. **11**, 287 (1999).
- [16] A.V. Kyuldjiev, Nucl. Phys. **B 243**, 387 (1984).
- [17] P.Vogel and J.Engel, Phys. Rev. **D 39**, 3378 (1989).
- [18] B. Kayser et al., Phys. Rev. **D 20**, 87 (1979).
- [19] R.C. Allen et al., Phys. Rev. Lett. **55**, 2401 (1985);  
R.C. Allen et al., Phys. Rev. **D 47**, 11 (1993).
- [20] For a recent review on solar neutrino experiments, see, for example,  
R.E. Lanou Jr., Nucl. Phys. **B (Procs. Suppl.) 77**, 55 (1999).
- [21] L. Wolfenstein, Phys. Rev. **D 17**, 2369 (1978);  
S.P. Mikheyev and A. Yu. Smirnov, Sov. J. Nucl. Phys. **42**, 1441 (1985).
- [22] C. Brogini et al., Nucl. Instrum. Methods **A311**, 319 (1992);  
C. Amsler et al., Nucl. Instrum. Methods **A 396**, 115 (1997).
- [23] J.M. Lattimer and J. Cooperstein, Phys. Rev. Lett. **61**, 23 (1988);  
R. Barbieri and R.N. Mohapatra, Phys. Rev. Lett. **61** 27 (1988);  
D. Notzold, Phys. Rev. **D 38**, 1658 (1988).
- [24] J. Bernstein et al., Phys. Rev. **132**, 1277 (1963);  
P. Sutherland et al., Phys. Rev. **D 12**, 2700 (1976);  
G. Raffelt, Phys. Rev. Lett. **64**, 2856 (1990).

- [25] J. Morgan, Phys. Lett. **B 102**, 247 (1981);  
M. Fukugita and S. Yazaki, Phys. Rev. **D 37**, 3817 (1987).
- [26] M.B. Voloshin, M.I. Vysotskii and L.B. Okun, Sov. Phys. JETP **64**, 446 (1986).
- [27] I.R. Barabanov et al., Astropart. Phys. **5**, 159 (1996);  
A.G. Beda et al., LANL preprint hep-ex/9706004 (1997).
- [28] B. Armbruster et al., Phys. Lett. **B 423**, 15 (1998).
- [29] H.C. Lee, Nucl. Phys. **A 294**, 473 (1978) ;  
T.W. Donnelly and R.D. Reccei, Phys. Rep. **50**, 1 (1979).
- [30] R.S. Raghavan and S. Pakvasa, Phys. Rev. **D 37**, 849 (1988).
- [31] C.C. Chang, C.Y. Chang, and G. Collins, Nucl. Phys. (Proc. Suppl.) **B 35**, 464 (1994).
- [32] M.W. Goodman and E. Witten, Phys. Rev. **D 31**, 3059 (1985);  
J. Ellis, R.A. Flores and J.D. Lewin, Phys. Lett. **B 212**, 375 (1988).
- [33] H. Ejiri, K. Fushimi and H. Ohsumi, Phys. Lett. **B 317**, 14 (1993).
- [34] P. Belli et al., Phys. Lett. **B 387**, 222 (1996).
- [35] D.B. Kaplan and A. Manohar, Nucl. Phys. **B 310**, 527 (1988);  
J. Bernabéu et al., Nucl. Phys. **B 378**, 131 (1992);  
G. Garvey et al., Phys. Rev. **C 48**, 1919 (1993);  
K. Kubodera and S. Nozawa, Int. J. Mod. Phys. **E 3**, 101 (1994).
- [36] ORLaND Proposal (1998).
- [37] L.M. Krauss, S.L. Glashow and D.N. Schramm, Nature **310**, 191 (1984).
- [38] C.Y. Chang, S.C. Lee and H.T. Wong, Nucl. Phys. **B** (Procs. Suppl.) **66**, 419 (1998).
- [39] J. Alarja et al., Nucl. Instrum. Methods **A 242**, 352 (1986);  
P. Kreutz et al., Nucl. Instrum. Methods **A 260**, 120 (1987).
- [40] C.L. Morris et. al., Nucl. Instrum. Methods **137**, 397 (1976);  
M.S. Zucker and N. Tsoupas, Nucl. Instrum. Methods **A299**, 281 (1990).
- [41] P. Jagam and J.J. Simpson, Nucl. Instrum. Methods **A 324**,

- [42] U. Kilgus, R. Kotthaus, and E. Lange, Nucl. Instrum. Methods **A 297**, 425, (1990);  
R. Kotthaus, Nucl. Instrum. Methods **A 329**, 433 (1993).
- [43] V.L. Alexeev et al., Nucl. Phys. **A248**, 249 (1975);  
L.A. Schaller, J. Kern and B. Michaud, Nucl. Phys. **A 165**, 415 (1971).
- [44] S. Charalambus, Nucl. Phys. **A 166**, 145 (1971);  
T. Suzuki, D.F. Measday, and J.P. Roalsvig, Phys. Rev. **C 35**, 2212 (1987);  
T. Kozlowski et al., Nucl. Phys. **A 436**, 717 (1985).
- [45] G. Cocconi and V. Cocconi Tongiorgi, Phys. Rev **84**, 29 (1951);  
S. Hayakawa, Phys. Rev **84**, 37 (1951).
- [46] R.S. Raghavan, Phys. Rev. Lett. **37**, 259 (1976);  
M. Avenier et al., Nucl. Phys. **B** (Proc. Suppl.) **28A**, 496 (1992).
- [47] R.S. Raghavan, Phys. Rev. Lett. **78**, 3618 (1997).
- [48] R. Chipaux et al., DAPNIA-SED-98-01, to be published in IEEE Trans Nucl. Sci.  
(1999).
- [49] P. Vilain et al., Phys. Lett. **B 335**, 246 (1994).

Properties	CsI(Tl)	NaI(Tl)	BGO	Liquid	Plastic
Density ( $\text{gcm}^{-3}$ )	4.51	3.67	7.13	0.9	1.0
Relative Light Yield	0.45	1.00 <sup>†</sup>	0.15	0.4	0.35
Radiation Length (cm)	1.85	2.59	1.12	$\sim 45$	$\sim 45$
dE/dx for MIP ( $\text{MeVcm}^{-1}$ )	5.6	4.8	9.2	1.8	1.9
Emission Peak (nm)	565	410	480	425	425
Decay Time (ns)	1000	230	300	2	2
Refractive index	1.80	1.85	2.15	1.5	1.6
Hygroscopic	slightly	yes	no	no	no

<sup>†</sup> Typical light yield for NaI(Tl) is about 40000 photons per MeV.

Table 1: Characteristic properties of the common crystal scintillators and their comparison with typical liquid and plastic scintillators.

Experiment	Savannah[8]	Kurtchatov[9]	Rovno[10]	NUMU[22]	TEXONO-CsI
Target	plastic scin.	fluorocarbon scin.	Si(Li)	CF <sub>4</sub> gas 5 bar	CsI(Tl) crystals
Fiducial mass	15.9 kg	103 kg	37.5 kg	18.4 kg	276 kg*
$\phi(\bar{\nu}_e)$ [ $10^{13} \text{ cm}^{-2}\text{s}^{-1}$ ]	2.2	0.27	2.0	1.0	0.56
Rel. Merit (flux $\times$ target)	1.0	0.7	1.8	0.44	3.1
Threshold (MeV)	1.5	3.1	0.6	0.5 (goal)	0.1 (goal)
Signal Events / Day	7.1	0.78	41	10 (expect)	200 (expect)
Event Rates Ratio					
Reactor OFF:(ON–OFF)	5.7	9.6	120	1 (goal)	<10 (goal)
Accuracy of $\sigma(\bar{\nu}_e e)$	29%	53%	49%	5% (goal)	5-10% (goal)
$\mu_\nu$ ( $10^{-10} \mu_B$ )	2-4 <sup>†</sup>	< 2.4	< 1.9	0.3 (goal)	0.3 (goal)

\* Based on a 481 kg (16 $\times$ 16 matrix) target with 1 veto layer and 5 cm veto buffer at both ends.

<sup>†</sup> Reanalysis of Savannah River experiment [17] indicates excess of events which can be interpreted as finite  $\mu_\nu$ .

Table 2: Characteristics of the previous and current  $\bar{\nu}_e$ -e scattering experiments.

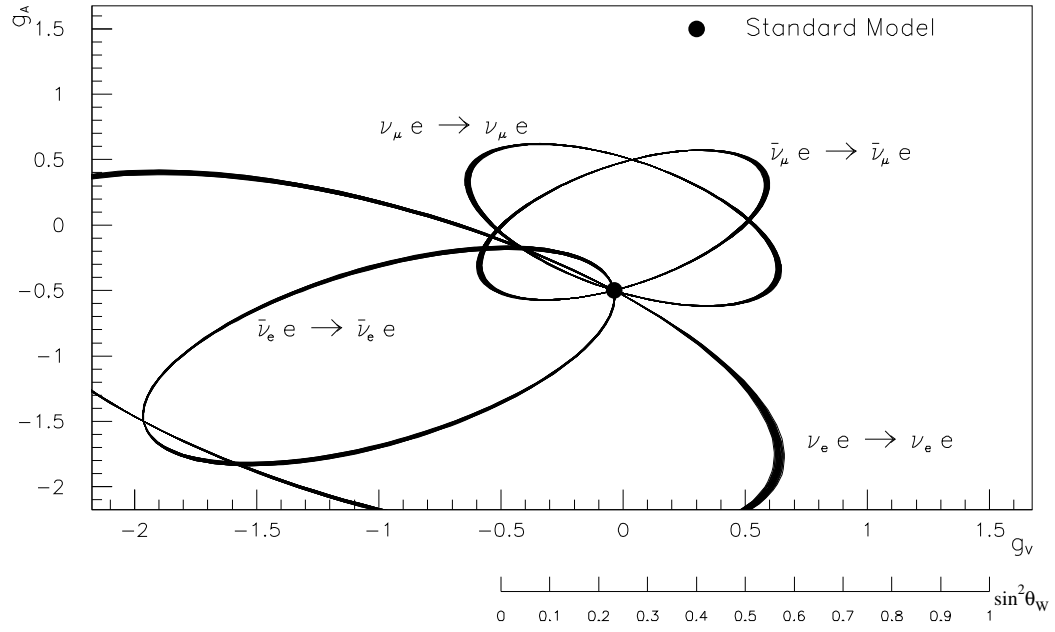
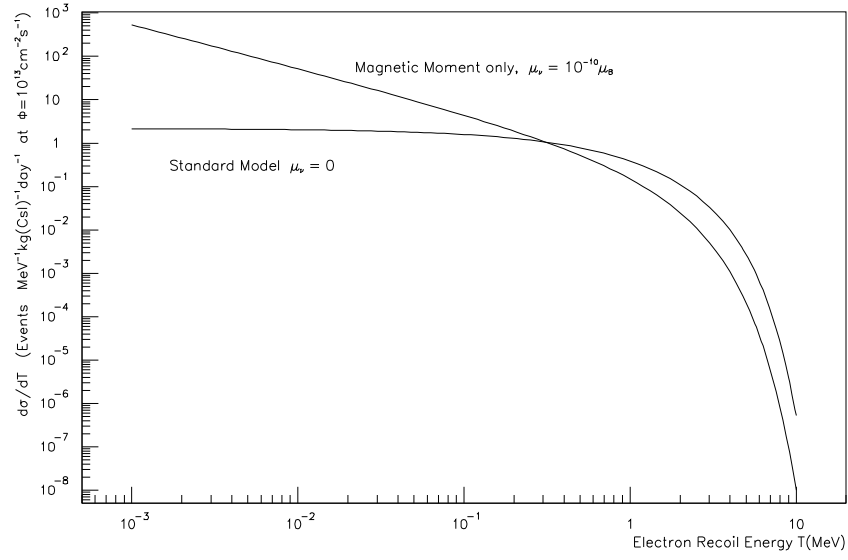


Figure 1: Sensitivities of typical  $(\nu_\mu e)$ ,  $(\bar{\nu}_\mu e)$ ,  $(\nu_e e)$  and  $(\bar{\nu}_e e)$  cross-section measurements to the different regions in the  $g_A$ - $g_V$  parameter space, showing their complementarity. The Standard Model values are denoted by the black dot.



(a)



(b)

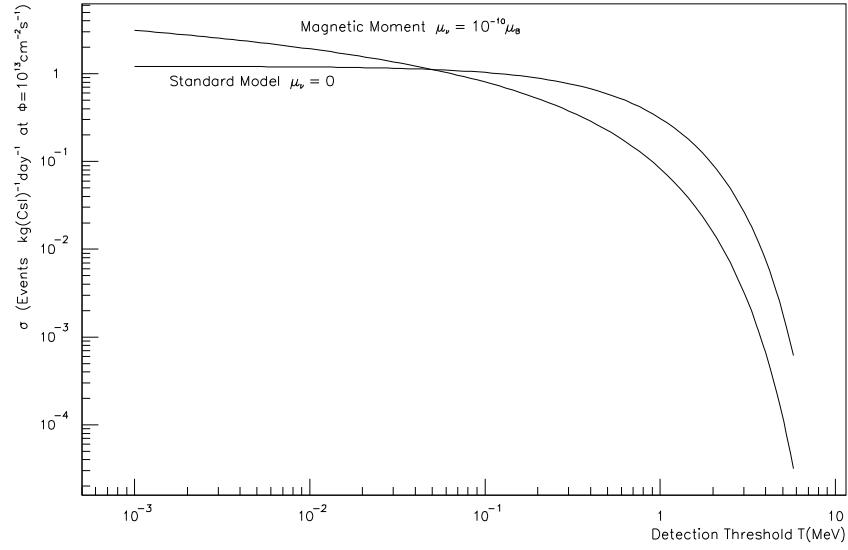


Figure 2: (a) Differential cross section showing the electron recoil energy spectrum in  $\bar{\nu}_e$ -e scatterings, and (b) expected event rates as a function of the detection threshold of the recoil electrons, at a reactor neutrinos flux of  $10^{13}\text{ cm}^{-2}\text{s}^{-1}$ , for the Standard Model processes and for the contribution due to a neutrino magnetic moment of  $10^{-10}$  Bohr magneton.

### Nuclear Power Plant II : Reactor Building

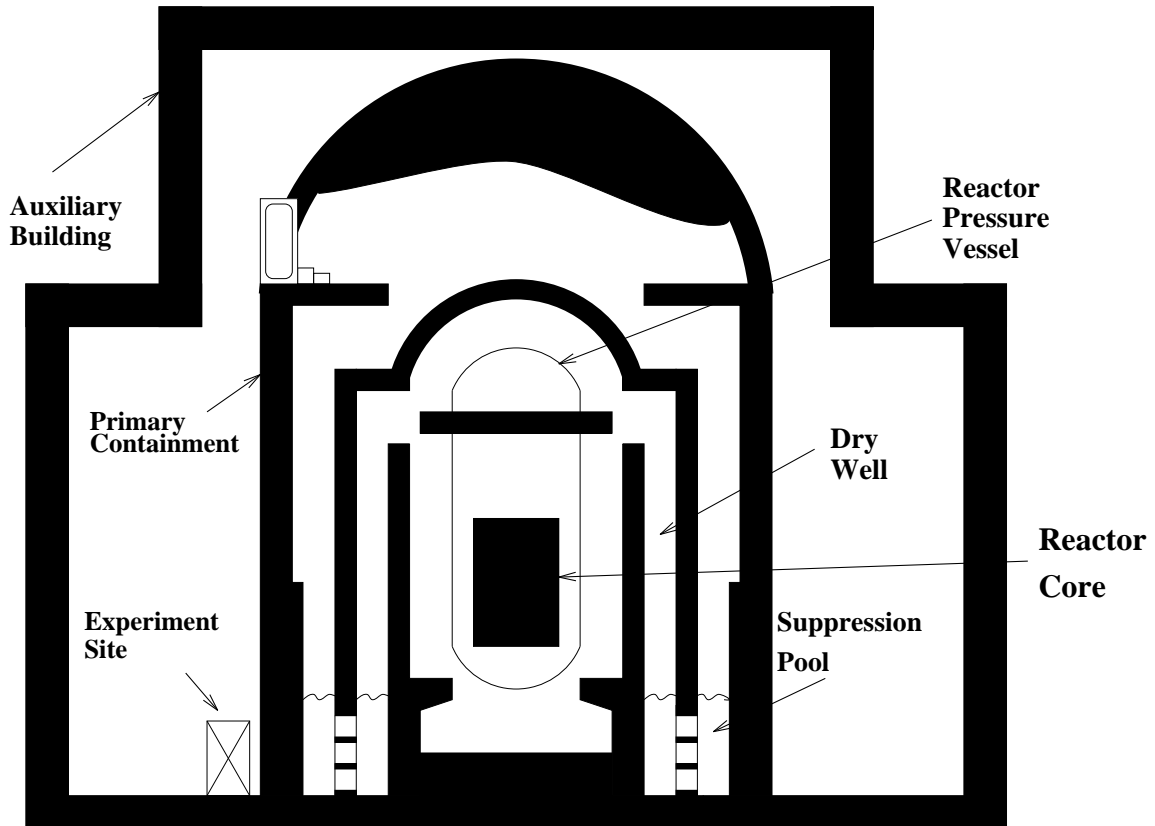


Figure 3: Schematic side view, not drawn to scale, of the NP2 Reactor Building, indicating the experimental site. The reactor core-detector distance is about 28 m.

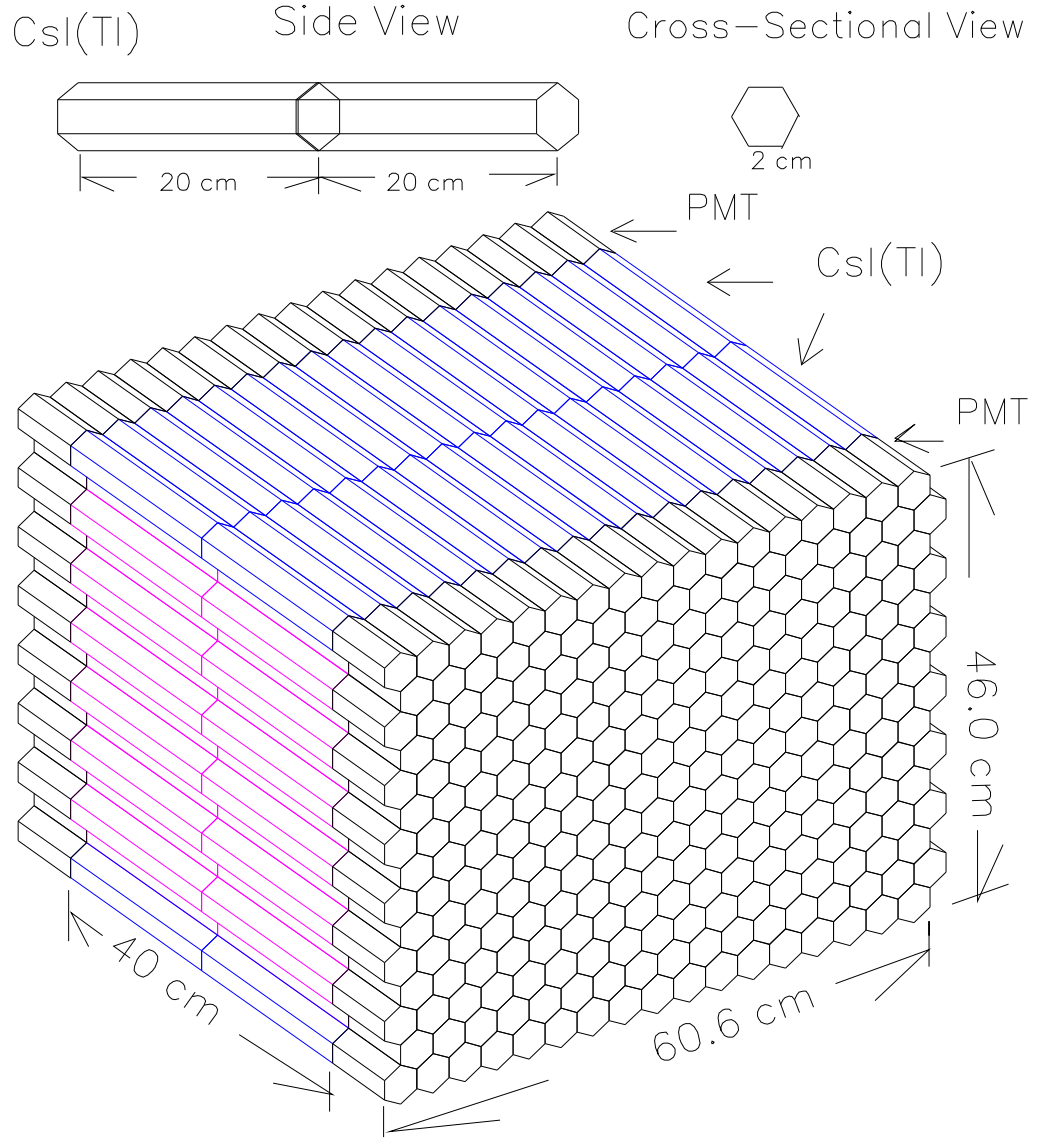


Figure 4: Schematic drawings of the CsI(Tl) target configuration, showing a 2(Width)X 17(Depth)X15(Height) matrix. Individual crystal module is 20 cm long with a hexagonal cross-section of 2 cm edge. Readout is performed by photo-multipliers at both ends.

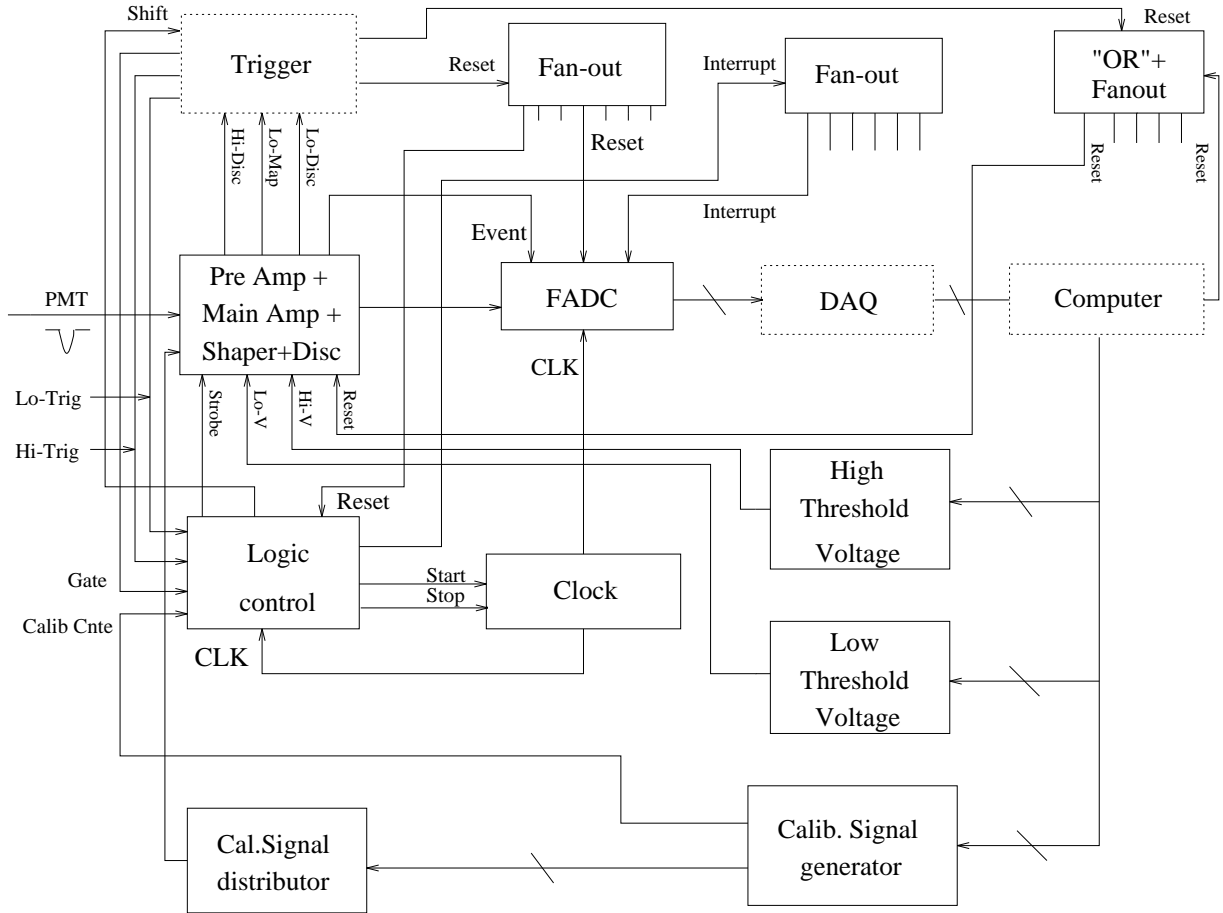


Figure 5: Schematic layout of the electronics system.

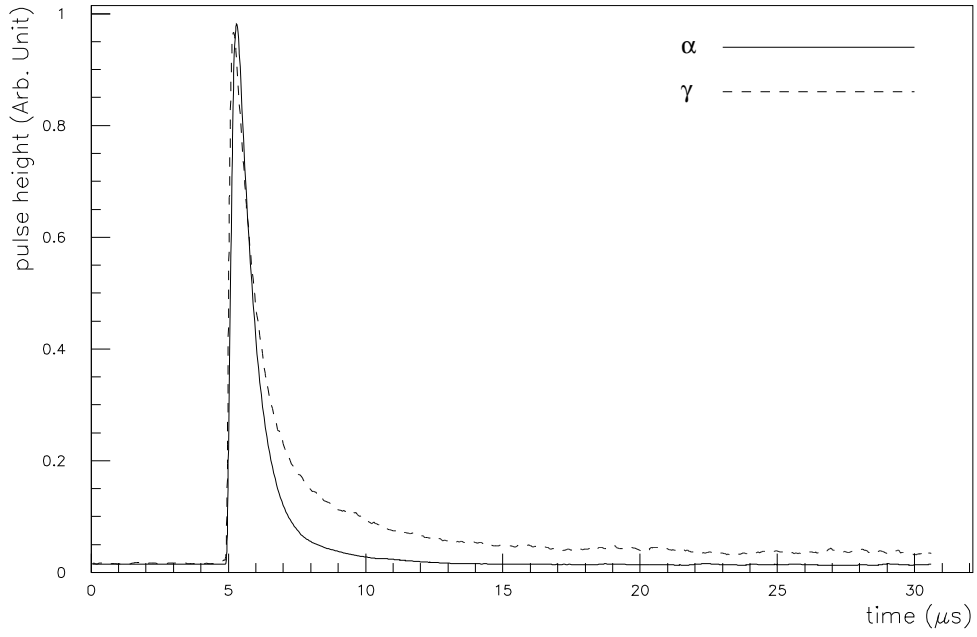


Figure 6: The average pulse shape of events due to  $\gamma$ -rays and  $\alpha$ -particles as recorded by the FADC module. Their different decay times provide pulse shape discrimination capabilities.

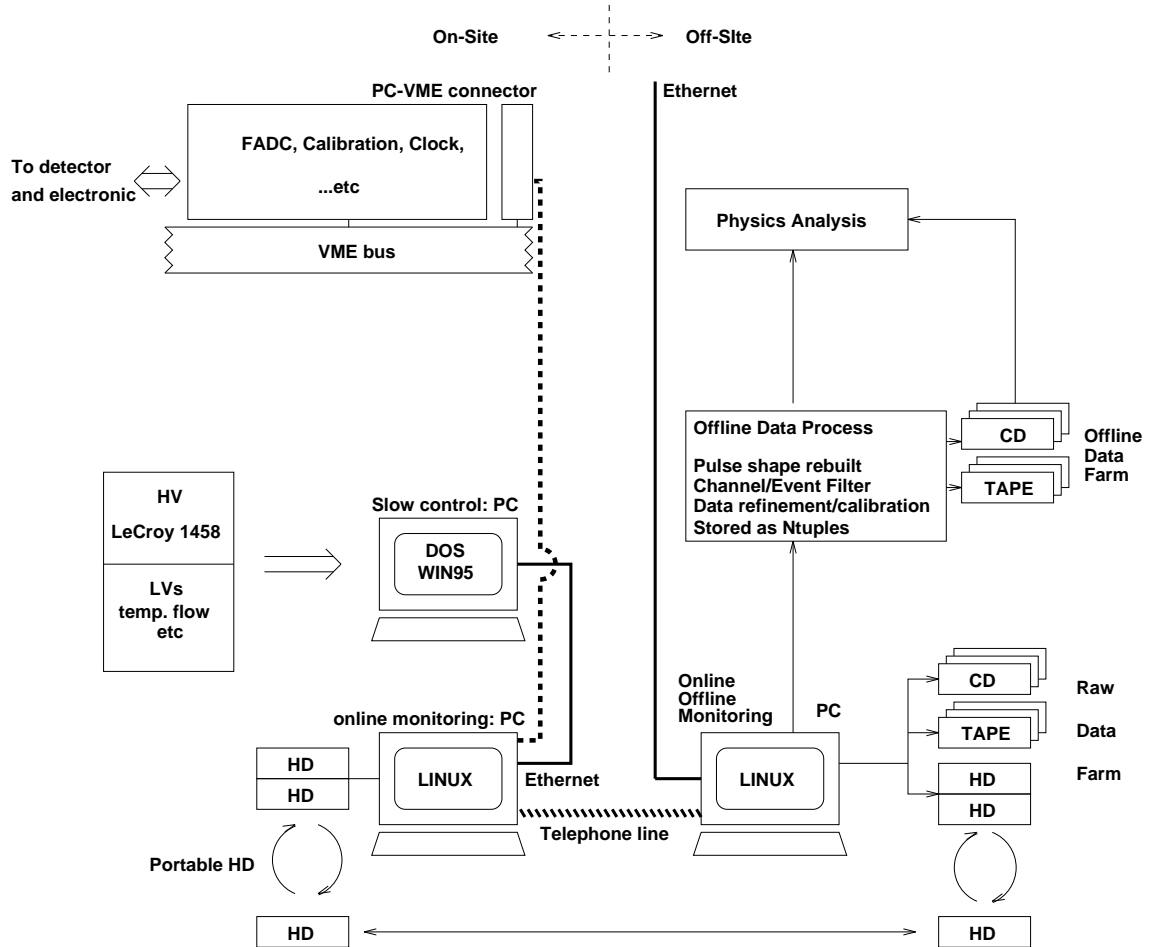


Figure 7: Schematic layout of the data acquisition and on-line monitoring systems, and its interfacing with the off-line software packages. A telephone line provides connection from home-base laboratories to the experimental site in the reactor building.

## Shielding Design

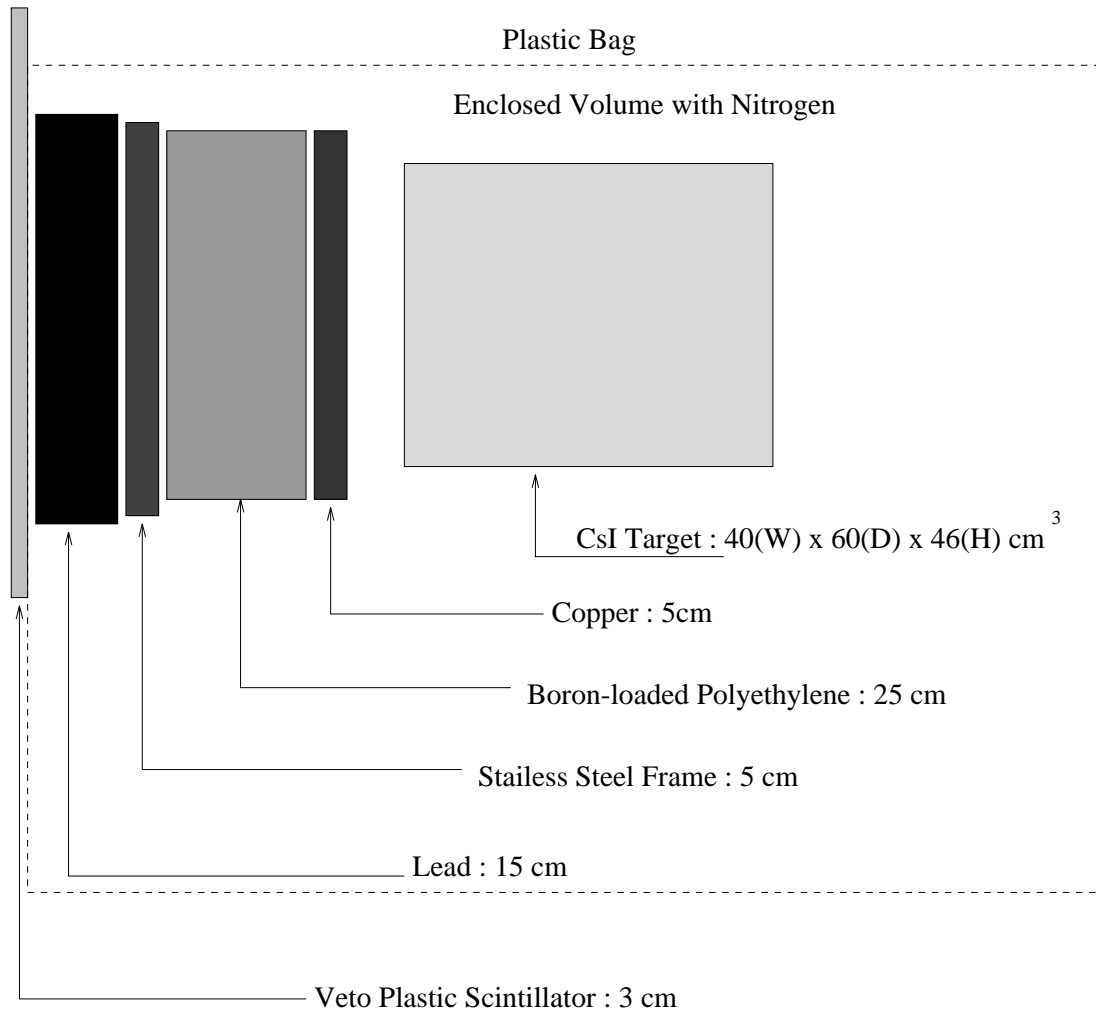


Figure 8: Schematic layout of the target and shielding configuration. The coverage is  $4\pi$  but only one face is shown.

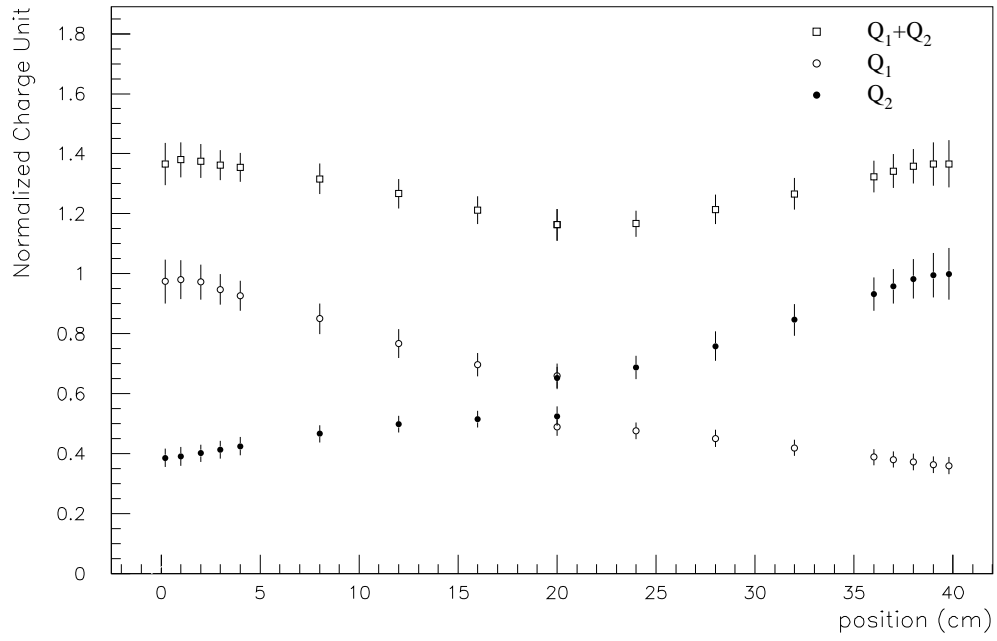


Figure 9: The measured variations of  $Q_1$ ,  $Q_2$  and  $Q_{\text{tot}} = Q_1 + Q_2$  along the longitudinal position of the crystal module. The charge unit is normalized to unity for both  $Q_1$  and  $Q_2$  at their respective ends. The error bars denote the width of the photo-peaks due to a  $^{137}\text{Cs}$  source.



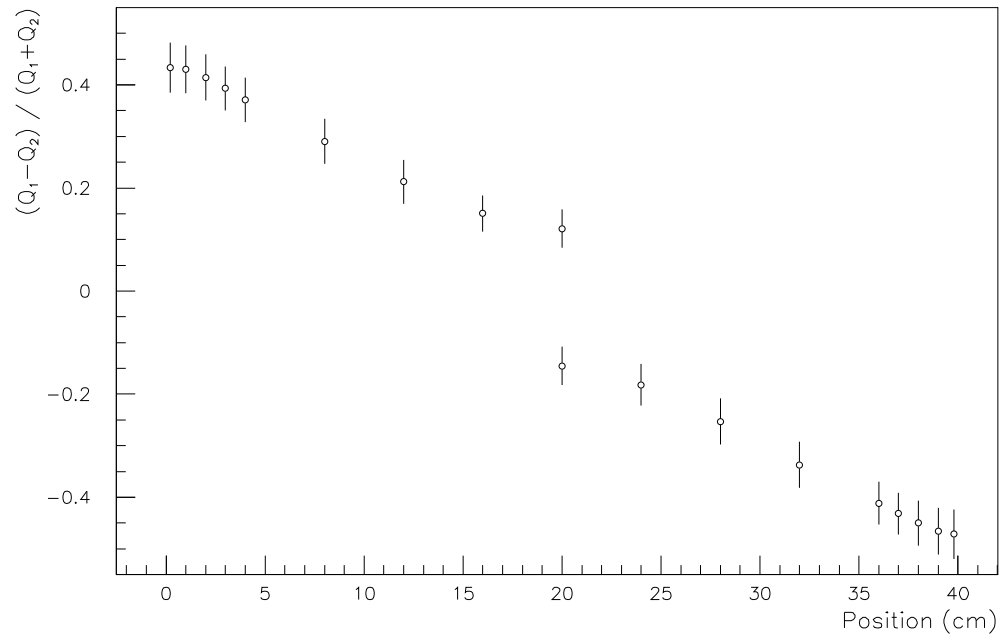


Figure 10: The variation of  $R = (Q_1 - Q_2)/(Q_1 + Q_2)$  along the longitudinal position of the crystal module, showing the capability to provide a position measurement.

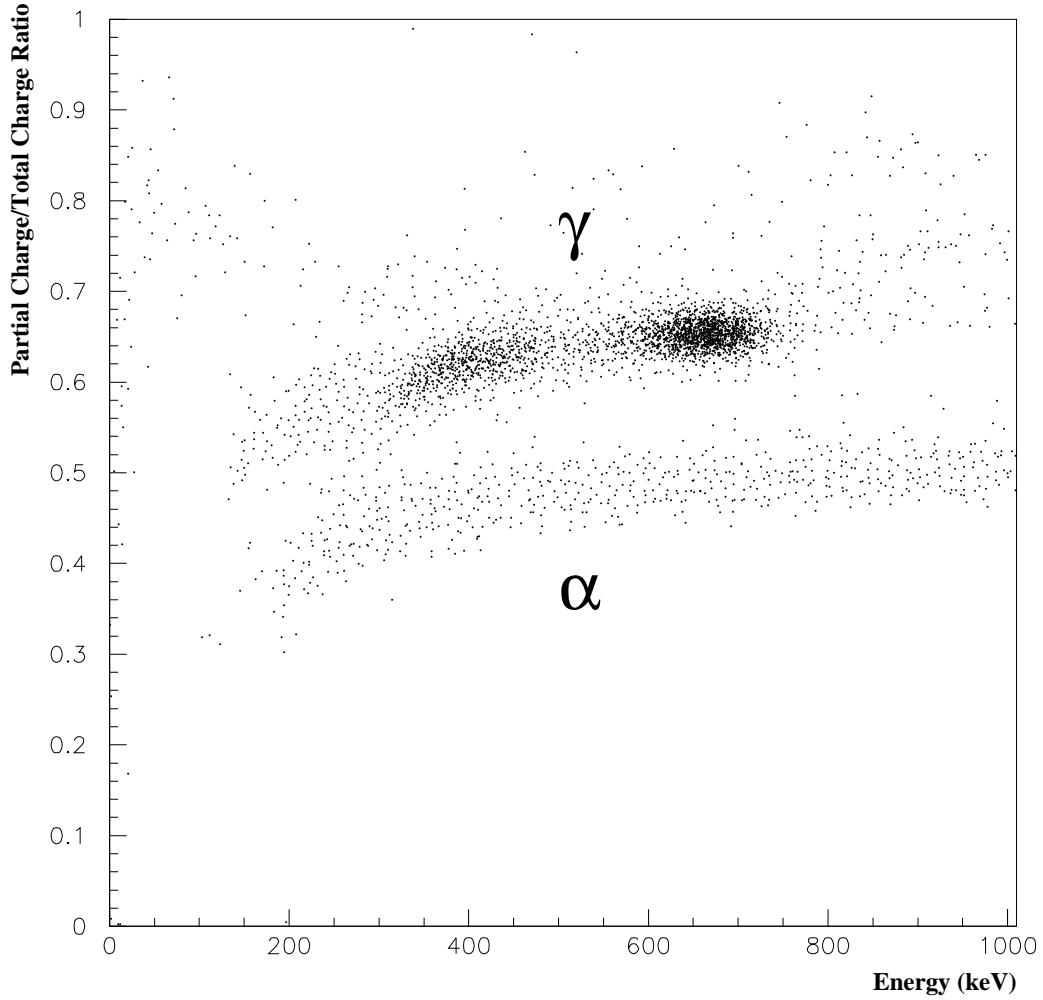


Figure 11: The partial charge/total charge ratio in a CsI(Tl) crystal as a function of energy, showing excellent pulse shape discrimination capabilities to differentiate events due to  $\alpha$ 's and  $\gamma$ 's. The  $\gamma$ -events are due to a  $^{137}\text{Cs}$  source, showing peaks at the full-energy and Compton edge regions. The  $\alpha$ -events are from the low-energy tails of an  $^{241}\text{Am}$ -Be source placed on the surface of the crystal.